CrossMark

COMMUNICATION

Bi₂Se₃/C Nanocomposite as a New Sodium-Ion Battery Anode Material
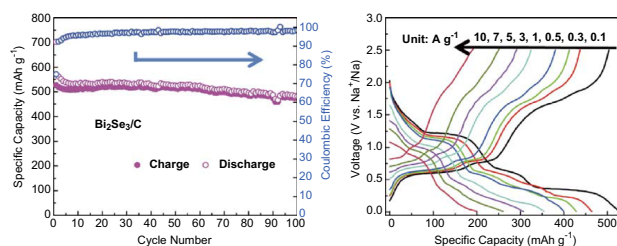
Lixin Xie[1] · Ze Yang[1] · Jingying Sun[1] · Haiqing Zhou[1] · Xiaowei Chi[2] · Hailong Chen[3] · Andy X. Li[4] · Yan Yao[2] · Shuo Chen[1]

Highlights

- Bi₂Se₃ was investigated as a novel sodium-ion battery anode material.
- Sodiation/desodiation mechanism of Bi₂Se₃ has been carefully investigated.
- Bi₂Se₃/C electrode demonstrates high cycling stability.

Abstract Bi₂Se₃ was studied as a novel sodium-ion battery anode material because of its high theoretical capacity and high intrinsic conductivity. Integrated with carbon, Bi₂Se₃/C composite shows excellent cyclic performance and rate capability. For instance, the Bi₂Se₃/C anode delivers an initial capacity of 527 mAh g^{-1} at 0.1 A g^{-1} and maintains 89% of this capacity over 100 cycles. The phase change and sodium storage mechanism are also carefully investigated.

Electronic supplementary material The online version of this article (https://doi.org/10.1007/s40820-018-0201-9) contains supplementary material, which is available to authorized users.

✉ Shuo Chen
schen34@uh.edu

1 Department of Physics and TcSUH, University of Houston, Houston, TX 77204, USA

2 Department of Electrical and Computer Engineering and Materials Science and Engineering Program, University of Houston, Houston, TX 77204, USA

3 The Woodruff School of Mechanical Engineering, Georgia Institute of Technology, Atlanta, GA 30332, USA

4 Clements High School, 4200 Elkins Dr, Sugar Land, TX 77479, USA

1 Introduction

Sodium-ion batteries (SIBs) have recently regained extensive research interest as alternatives to lithium-ion batteries (LIBs) for energy storage owing to the low cost and abundance of Na [1–5]. The lack of high energy density anode materials has impeded the progress of SIBs for a long time [6]. Developing suitable anode materials for SIBs with both high capacity and long cycle life is highly desired. Among anode materials, alloying-type materials [7] have attracted much attention. For example, Sn, Sb, and

Bi can reversibly alloy with Na^+ and provide high theoretical gravimetric capacities (> 300 mAh g^{-1}), which far exceed the capacities of carbonaceous materials and Ti-based materials. The accompanying challenge for alloying-type materials is the large volume expansion when alloying with Na^+. Bi displays a relatively small volume expansion (ca. 250% expansion from Bi to Na_3Bi), compared to Sn (ca. 420% expansion from Sn to $Na_{3.75}Sn$) and Sb (ca. 293% expansion from Sb to Na_3Sb) [8], which is beneficial for a stable anode [9]. The voltage plateau is also an important criterion in evaluating an electrode material. A low operating voltage for anode materials can endow a cell with a high operation voltage. However, Na plating, dendrite formation, and electrolyte decomposition occur on the anode side when the discharge voltage approaches 0 V, as is often the case for hard carbon anodes [10–12]. The plateaus of Bi between 0.3 and 0.9 V versus Na^+/Na are favorable for maintaining a high operation voltage and avoiding the aforementioned detrimental effects [13, 14].

Sulfides and selenides have been actively investigated because their conversion reactions offer high capacities for ion storage [15–18]. Recently, the Bi-based compound Bi_2S_3 has been synthesized and displayed a high Na storage capacity [19, 20]. However, the rate capacity was unsatisfactory, limited by the low intrinsic conductivity of sulfides [15]. Bi_2Se_3 displays an electrical conductivity two orders of magnitude higher than that of Bi_2S_3 [21], which can improve the electron transport. In addition, the shuttle effect is relieved for selenides compared to sulfides [22]. Moreover, Bi_2Se_3 has a high density of 7.47 g cm^{-3} [21], permitting the opportunity to fabricate small-sized devices with high volumetric capacities (theoretically 3667 mAh cm^{-3}). Bi_2Se_3 has been applied in LIBs and exhibited excellent electrochemical storage ability for Li^+. Several Bi_2Se_3 nanostructures, such as nanosheets and microrods, have been designed for Li^+ storage [23, 24]. Furthermore, high free electron densities can effectively improve the rate capability; thus, doping strategies have been employed to create S-doped and In-doped Bi_2Se_3 [25–27]. Despite the good electrochemical performance in Li^+ storage, Bi_2Se_3 has not been reported as an anode material for SIBs.

Downsizing the bulk material to nanoscale and integrating carbon with it can improve the electrochemical performance, including the rate capability and cyclability, by the shorter diffusion distances, more abundant reaction sites on the large surface area, and additional space for expansion [28–31]. Carbon can stabilize the nanomaterial and provide an interconnected network for electron transport as well, and the voids in the carbon can accommodate volume expansion and allow permeation of the electrolyte for fast Na^+ transport [32–34].

In our study, a simple high-energy ball milling (HEBM) method was adopted to synthesize Bi_2Se_3 and Bi_2Se_3/C

nanocomposite. The Bi_2Se_3/C nanocomposite delivers an initial reversible capacity of 527 mAh g^{-1} at 0.1 A g^{-1} with 89% retention over 100 cycles. The phase changes during cycling were investigated by ex situ X-ray diffraction (XRD) to reveal the Na storage mechanism. The rational material design combined with effective synthetic protocol is important and this work is expected to shed light on future work on developing excellent anode materials for SIBs.

2 Experimental

2.1 Synthesis Process

The synthesis of Bi_2Se_3 and Bi_2Se_3/C was performed by HEBM. Bi (Alfa Aesar, 99.999%) and Se (Alfa Aesar, 99.999%) in a molar ratio of 2:3 were sealed in an Ar-filled stainless steel jar and then ball milled for 10 h at 1200 rpm (Spex 8000 M) to form phase-pure Bi_2Se_3 powder. Graphite powders were milled for 48 h beforehand. Then, the milled graphite was added to Bi_2Se_3 powders in the weight ratio of 2:8 and ball milled for another 6 h to form the carbon-integrated Bi_2Se_3 nanocomposite.

2.2 Material Characterization

The phases were investigated by XRD on a Rigaku SmartLab diffractometer with a Cu Kα source at the scan rate of 5 deg. min^{-1}. The morphology was studied under scanning electron microscopy (SEM, LEO 1525). The nanostructures and the diffraction patterns were characterized by transmission electron microscopy (TEM, JEOL 2010F, operated under 200 kV). The elemental mapping was collected by energy-dispersive X-ray spectroscopy (EDS) (attached to the TEM). X-ray photoelectron spectroscopy (XPS) measurements were performed on a PHI Quantera XPS instrument. To confirm the carbon content, the samples were heated at 10 °C min^{-1} from room temperature to 600 °C in thermogravimetric analysis (TGA, Q500).

2.3 Electrochemical Measurements

Coin cells (CR 2025) with Bi_2Se_3 or Bi_2Se_3/C as the active material were assembled for battery tests. A slurry was made by mixing 70 wt% active material, 20 wt% carbon black, and 10 wt% polyacrylic acid (PAA) and then coated on a Cu foil to form the working electrodes, followed by drying at 60 °C under vacuum overnight. To prepare the electrolyte, 1 mol L^{-1} $NaClO_4$ was dissolved in propylene carbonate/ethylene carbonate (1:1 in volume) with 5 wt% fluoroethylene carbonate (FEC) as an additive. The loading

of the active materials was 1.4 ± 0.2 mg cm^{-2} for the Bi$_2$Se$_3$/C electrode and 1.5 ± 0.3 mg cm^{-2} for the Bi$_2$Se$_3$ electrode. Homemade Na lumps and glass fibers were applied as the reference/counter electrodes and the separators, respectively. The electrochemical measurements of the cells were performed galvanostatically between 0.01 and 2.5 V versus Na/Na$^+$ on a Land CT2001A battery tester. Cyclic voltammetry (CV) curves were swept at 0.1 mV s^{-1} on a BioLogic SP-200 electrochemical workstation. Electrochemical impedance spectroscopy (EIS) was measured from 100 kHz to 100 mHz with a voltage amplitude of 5 mV.

3 Results and Discussion

Figure 1 displays the structural and morphological characterization details of Bi$_2$Se$_3$ and Bi$_2$Se$_3$/C. The XRD patterns of Bi$_2$Se$_3$ and Bi$_2$Se$_3$/C are shown in Fig. 1a. The ball milled Bi$_2$Se$_3$ and Bi$_2$Se$_3$/C display the same XRD patterns, which match well with the pure rhombohedral

phase (space group $R\bar{3}m$ (166), JCPDS card No. 33-0214). After ball milling with carbon for another 6 h, the peaks of Bi$_2$Se$_3$/C become broader, indicating that smaller nanocrystals are produced. The crystal structure is again confirmed in the electron diffraction patterns of Fig. 1b, with the rings well indexed as the planes (0 0 6), (1 0 1), (0 1 5), (0 1 8), and (1 0 10) of rhombohedral-phase Bi$_2$Se$_3$. The TEM image in Fig. 1c and high-resolution TEM image in Fig. 1d show that the secondary Bi$_2$Se$_3$ particles are composed of well-developed nanocrystals with sizes ranging from a few nanometers to tens of nanometers. Figure 1e, f demonstrate that the Bi$_2$Se$_3$ nanocrystals are well encapsulated and uniformly distributed in the carbon matrix after integration with carbon. The primary nanocrystal sizes are approximately 5–20 nm, much smaller than those of as-synthesized Bi$_2$Se$_3$ because the carbon matrix can well separate and stabilize Bi$_2$Se$_3$ nanocrystals [32]. To reflect nanocrystal sizes across the samples, additional high-resolution TEM images are provided in Fig. S1. The particle sizes of the Bi$_2$Se$_3$/C nanocomposite also grow finer due to the separation of
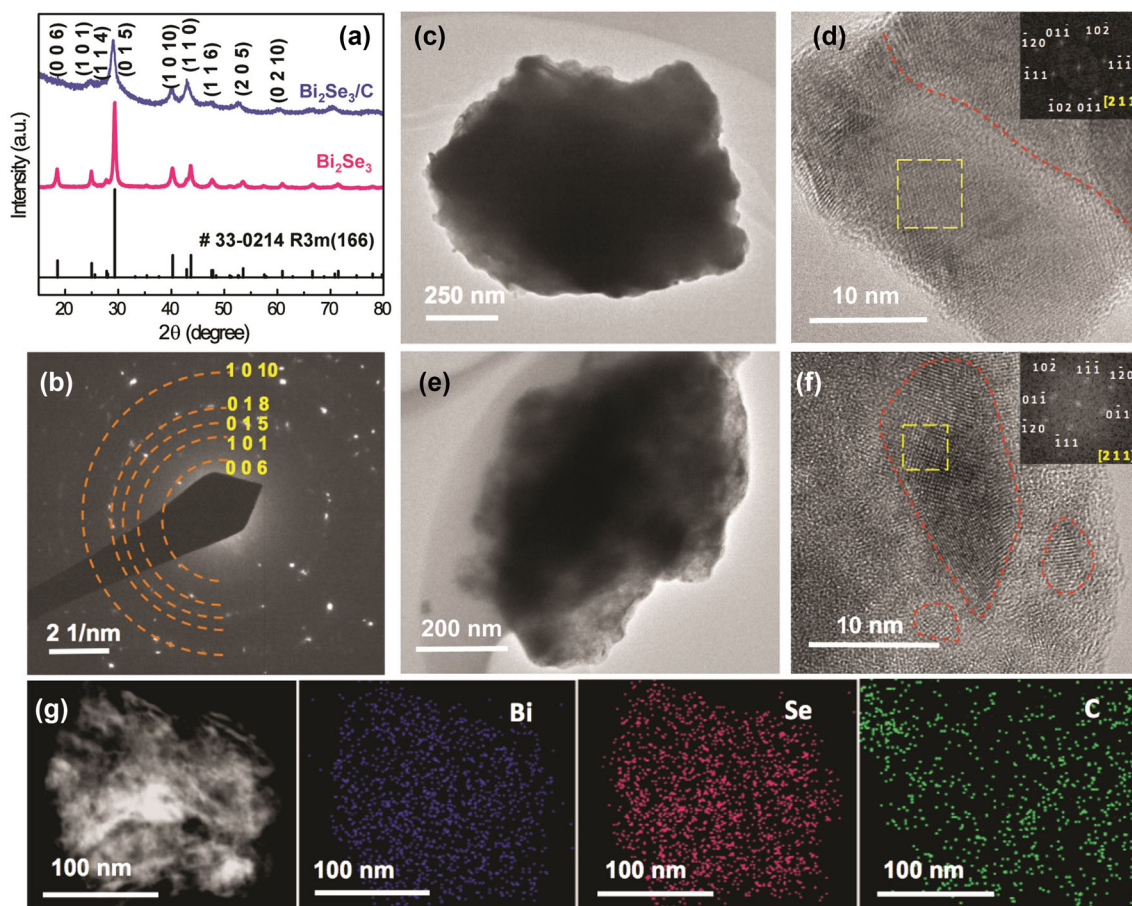

Fig. 1 **a** XRD patterns of as-synthesized Bi$_2$Se$_3$ and Bi$_2$Se$_3$/C. **b** The diffraction pattern of Bi$_2$Se$_3$. **c** Low- and **d** high-resolution TEM images of Bi$_2$Se$_3$. **e** Low- and **f** high-resolution TEM images of Bi$_2$Se$_3$/C. **g** Scanning TEM (STEM) image and its corresponding elemental (Bi, Se, and C) mappings

carbon compared to those of bare Bi_2Se_3, as observed in the SEM images (Fig. S2). Clear fringes of the crystal planes of Bi_2Se_3 can be found in Fig. 1f, indicating that the Bi_2Se_3 maintains good crystallinity in the carbon composite. In Fig. 1g, the uniform distribution of the elements Bi, Se, and C is confirmed by the EDS mapping. The carbon content of the composite is further confirmed to be 20.7 wt% by the TGA test (Fig. S3).

The half-cell of Bi_2Se_3/C was cycled at a scan rate of 0.1 mV s^{-1} within 0.01–2.5 V versus Na$^+$/Na and the I–V curves are shown in Fig. 2a. Three cathodic peaks at 1.04, 0.52, and 0.27 V and four anodic peaks at 1.88, 1.7, 0.79, and 0.67 V are depicted in the first cycle. The peak positions are analogous to those in Bi_2S_3 anode because of the similar properties between S and Se as chalcogens [14, 19, 20]. In the cathodic scan, Bi and Na_2Se form at 1.04 V [19, 20], followed by the sodiation of Bi at lower voltages of 0.52 and 0.27 V [14]. In the reverse scan, desodiation of the Na–Bi alloy occurs at 0.67 and 0.79 V [14], then $NaBiSe_2$ is formed at 1.7 and 1.88 V [19, 20, 35]. The peak at 1.04 V in the first cycle is slightly shifted to 1.14 V in the following cycle. Other than this shift, the CV curves overlap very well, which indicates a

highly reversible Na storage kinetics. Figure S4 also displays the CV curve of Bi_2Se_3. The same characteristics are observed in the CV curves of Bi_2Se_3 and Bi_2Se_3/C, which indicate that integrating carbon does not affect the sodiation process of Bi_2Se_3. However, integrating carbon does improve the stability of the electrode, which is evidenced by the obvious decrease in the peak intensities of bare Bi_2Se_3 over CV cycling.

The cyclic performances of Bi_2Se_3 and Bi_2Se_3/C at 0.1 A g^{-1} and the related Coulombic efficiency of the Bi_2Se_3/C anode are shown in Fig. 2b. Alloying and conversion anodes often show lower Coulombic efficiencies than intercalation anodes. At the first cycle, the Bi_2Se_3 and Bi_2Se_3/C anodes both display reasonably high Coulombic efficiencies (> 75%), indicating higher utilization of Na$^+$ than most alloying anodes. With carbon integrated, the reversible capacity of Bi_2Se_3/C anode (527 mAh g^{-1}) is somewhat comprised compared to the capacity of 557 mAh g^{-1} for the Bi_2Se_3 anode at the first cycle. In the following cycles, however, the Bi_2Se_3/C anode exhibits much improved stability, reaching a steady value of 510 mAh g^{-1} within five cycles and retaining 89% of the initial capacity over 100 cycles, while the Bi_2Se_3 anode
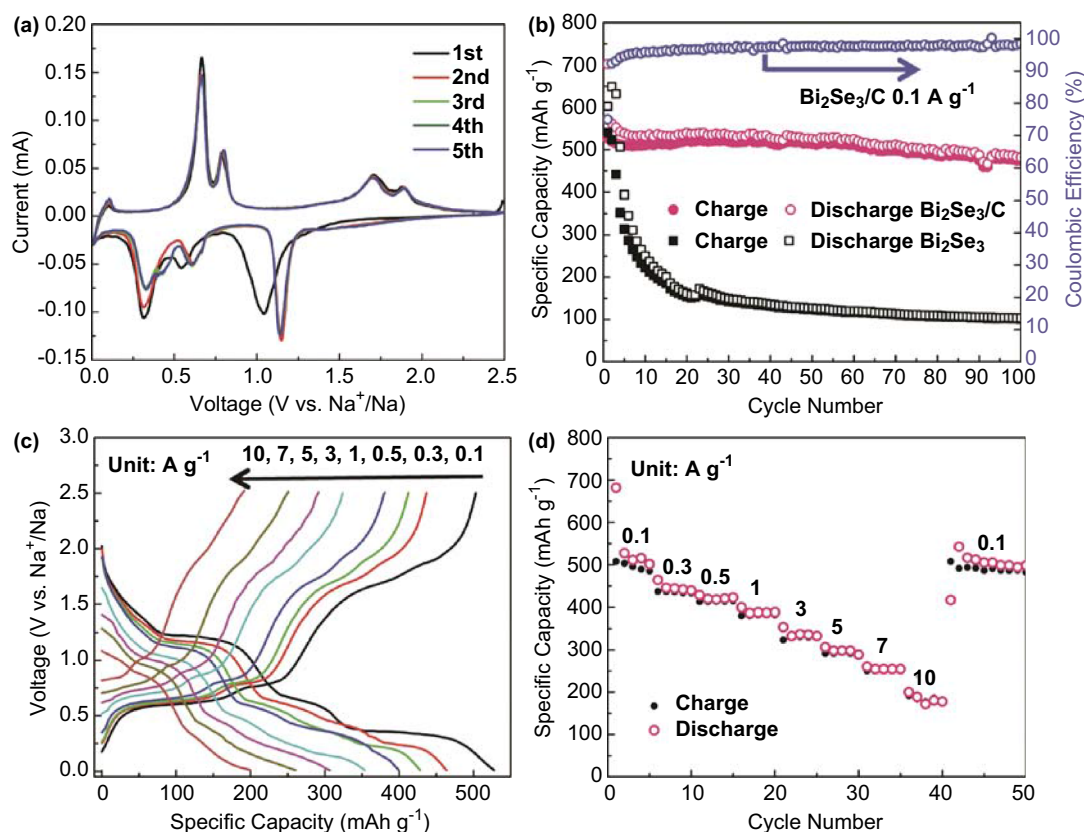

Fig. 2 Studies of electrochemical properties of the Bi_2Se_3/C anode for SIBs. a CV curves of the Bi_2Se_3/C anode at 0.1 mV s^{-1}. b Cyclic performance of Bi_2Se_3/C and Bi_2Se_3 anodes at 0.1 A g^{-1} and the related Coulombic efficiency of Bi_2Se_3/C anode. c Discharge/charge profiles and d rate performance of Bi_2Se_3/C anode at different current densities

displays a fast decay in capacity to below 200 mAh g^{-1} within 20 cycles. At a higher current density of 0.5 A g^{-1}, the Bi$_2$Se$_3$/C anode still shows high stability with an initial capacity of 445 mAh g^{-1} after the first two cycles at 0.1 A g^{-1} and that of 383 mAh g^{-1} over 180 cycles (Fig. S5). The cyclic performance of Bi$_2$Se$_3$/C is superior to those of other Bi-based materials and competitive with many typical anode materials (Table S1) [36–41]. Although the initial capacity of Bi$_2$Se$_3$/C is not extremely high compared to those of similar materials reported, the unique advantage of this composite is its stability in long-term cycling. For example, at 0.1 A g^{-1}, the capacity of 470 mAh g^{-1} for Bi$_2$Se$_3$/C composite at the 100th cycle is more than triple that of Bi@C microspheres [42] and ca. 50% higher than that of Bi$_2$S$_3$ nanorods at the 40th cycle [19]. Figure 2c shows the voltage profiles of the Bi$_2$Se$_3$/C anode for a wide range of discharge/charge rates between 0.01 and 2.5 V versus Na$^+$/Na. At the low current density of 0.1 A g^{-1}, the plateaus can be clearly identified with three discharge plateaus and four charge plateaus, corresponding to the peaks in the CV curves. The discharge/charge profiles maintain analogous shapes and plateaus even at very high current densities, indicating the fast reaction kinetics of the Na storage process. The details of the fast reaction kinetics may be ascribed to the fast capacitive contribution, as discussed later. Figure 2d shows the excellent rate capability of Bi$_2$Se$_3$/C as an anode material for SIBs. Remarkably, it delivers the high capacities of 500, 445, 415, 384, 332, 298, 255, and 186 mAh g^{-1} at 0.1, 0.3, 0.5, 1, 3, 5, 7, and 10 A g^{-1}, respectively. To confirm the high reversibility, 0.1 A g^{-1} is applied again after cycling at 10 A g^{-1}, and the capacity returns to its previous level as expected. The rate capacities of Bi$_2$Se$_3$/C are competitive with those of typical anode materials listed in Table S2 and the performance is better at high current densities. The volumetric capacity is also an important consideration for practical application; that of the Bi$_2$Se$_3$/C electrode reaches 1064 mAh cm^{-3}, calculated by multiplying the volumetric density of Bi$_2$Se$_3$/C (2.02 g cm^{-3}) with the gravimetric capacity (527 mAh g^{-1}) at 0.1 A g^{-1}.

To explore the insights of sodiation/desodiation mechanism of Bi$_2$Se$_3$, ex situ XRD was conducted. After charging/discharging, the electrodes were removed from the cells in a glove box and covered with Kapton tapes to avoid oxidation. The sampling points were chosen in reference to the dQ/dV curves in Fig. 3a. When the anode is sodiated to 0.86 V from the open-circuit voltage, the Bi$_2$Se$_3$ characteristic peak disappears while Bi peaks appear with Na$_2$Se [14]. The XRD patterns of Bi and Na$_2$Se are maintained when the material is discharged to a low voltage of 0.47 V. In this process, the intercalation of Na$^+$ into Bi may occur. The phase of NaBi appears at 0.01 V, indicating that alloying reaction occurs at the complete
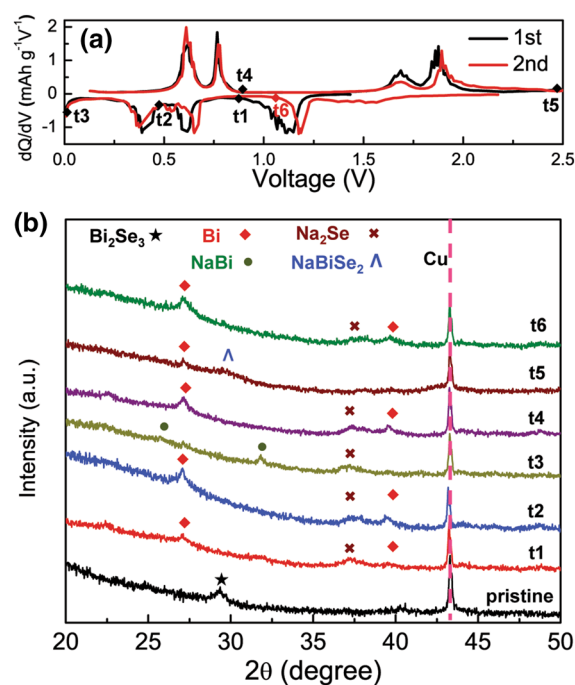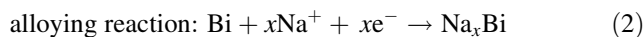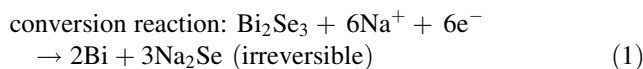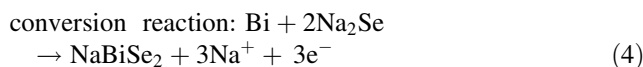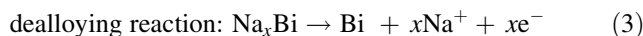

Fig. 3 a dQ/dV plots for the first two cycles and b ex-situ XRD results of the Bi$_2$Se$_3$/C anode

sodiation state [8, 43]. In the desodiation process, Bi dealloys with Na$^+$, evidenced by the appearance of the Bi phase at 0.88 V. However, even at the highest potential of 2.5 V, the Bi$_2$Se$_3$ phase does not recover; instead, NaBiSe$_2$ with Bi phases are formed [19]. The irreversible Bi$_2$Se$_3$ change can also explain the peak shifting from 1.04 V in the first cycle to 1.14 V in the following cycles in the I–V curves of Fig. 2a. When the electrode is again sodiated to 1.05 V at the second cycle, diffraction patterns corresponding to Bi and Na$_2$Se appear again. In summary, the phase changes during cycling can be listed as the following four steps:

Sodiation process:

conversion reaction: Bi$_2$Se$_3$ + 6Na$^+$ + 6e$^-$
$$\rightarrow 2Bi + 3Na_2Se \text{ (irreversible)} \qquad (1)$$

alloying reaction: $Bi + xNa^+ + xe^- \rightarrow Na_xBi$ (2)

Desodiation process

dealloying reaction: $Na_xBi \rightarrow Bi + xNa^+ + xe^-$ (3)

conversion reaction: Bi + 2Na$_2$Se
$$\rightarrow NaBiSe_2 + 3Na^+ + 3e^- \qquad (4)$$

In addition to XRD analysis, XPS was also applied to provide a more comprehensive understanding of the materials and the electrochemical process, because XPS is sensitive to the surface within the depth of ca. 5 nm. Figure S7 displays the XPS survey spectrum and high-resolution spectra of Bi 4f and Se 3d for Bi$_2$Se$_3$/C electrode.

The peaks at 163.7 and 158.4 eV are assigned to Bi $4f_{5/2}$ and Bi $4f_{7/2}$, respectively. The peaks at 54.3 and 53.5 eV correspond to Se $3d_{3/2}$ and Se $3d_{5/2}$ in Bi_2Se_3, respectively, confirming the successful synthesis of Bi_2Se_3 [44]. In addition, the peaks related to BiO_x and SeO_x are also found, indicating oxidation happens at the surface [44]. The solid electrolyte interface (SEI) compositions were also investigated by comparing the electrode before and after one cycle. Figure 4 indicates significant changes in the C 1s and F 1s spectra. The pristine electrode has a strong signal at 284.6 eV related to the carbon bonds of graphite or carbon black, and the small peaks at 285.3, 285.9, and 288.8 eV correspond to $-\underline{C}H_2-$, $-\underline{C}H-COONa$, and R–$\underline{C}OONa$ of the PAA binder [9, 45]. After one cycle, several new peaks are formed in the higher binding energy region and the strong signal at 284.6 eV related to graphite and carbon black disappears, indicating the formation of the SEI film on the surface. The signals from 286.0 to 289.5 eV are assigned to the $-\underline{C}-O-$ and $-\underline{C}=O-$ species of the SEI film and the peak at 291.1 eV arises from Na_2CO_3 of the SEI film [9, 46]. The signal related to F 1s appears after one cycle, indicating that the SEI film contains F from the decomposition of FEC.

The reaction kinetics can be revealed by EIS and the EIS spectra of Bi_2Se_3/C electrode and Bi_2Se_3 electrode are displayed in Fig. 5a. The intercept with the Z_{real} axis at high frequency represents the electrolyte and contact resistance (R_s), while the semicircles at medium frequency

are related to the SEI resistance (R_f) and electrolyte/electrode charge transfer resistance (R_{ct}) [47]. The equivalent circuit model for the fitting is shown in the inset of Fig. 5a with the fitting results listed in Table S3. R_{ct} of the Bi_2Se_3/C electrode decreases significantly from 661.4 to 81.4 Ω after cycling benefited from the reconstructed porous structure with close connections, as seen under SEM (Fig. S8) [48]. On the contrary, the EIS spectra of Bi_2Se_3 display a large R_{ct} increase after cycling due to the contact loss. For the Bi_2Se_3 electrode after cycling, large aggregates are formed with rough surfaces and loose contact between particles. In addition, the R_f increase of 19.9 Ω for the Bi_2Se_3 electrode is more significant than that of 6.8 Ω for the Bi_2Se_3/C electrode, caused by the fracture and the continuous growth of a thick SEI layer in the Bi_2Se_3 electrode.

For nanomaterials with large surface areas, surface-induced capacitive processes can have significant effects and improve the charge/discharge capability [49–51]. The b value is often used as an index to estimate the surface-induced capacitive contribution. According to $i = av^b$, where i is the current response at the scan rate v, the b value can be readily fitted by $\log(i) - \log(v)$ linear plots. The b value can vary from 0.5 to 1. The capacitive process dominates when the b value is close to 1, while diffusion-controlled processes dominate when the b value approaches 0.5. Figure 5b shows the I–V curves at different scan rates for the Bi_2Se_3/C electrode; the relations of $\log(i)$ and
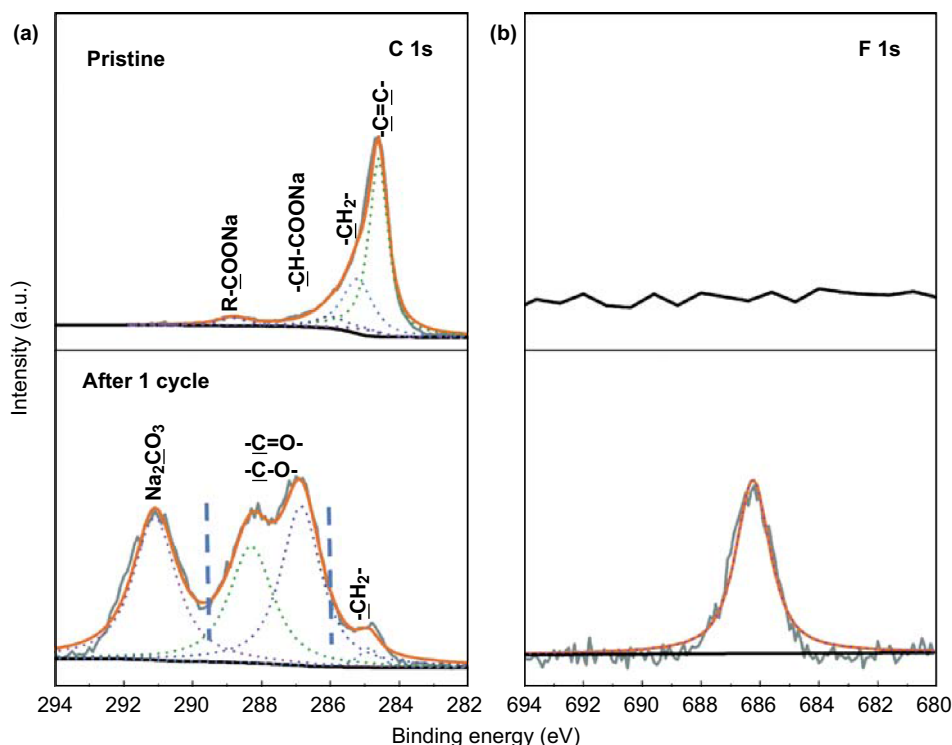
Fig. 4 High-resolution XPS spectra **a** C 1s and **b** F 1s of the Bi_2Se_3/C electrode before and after one cycle

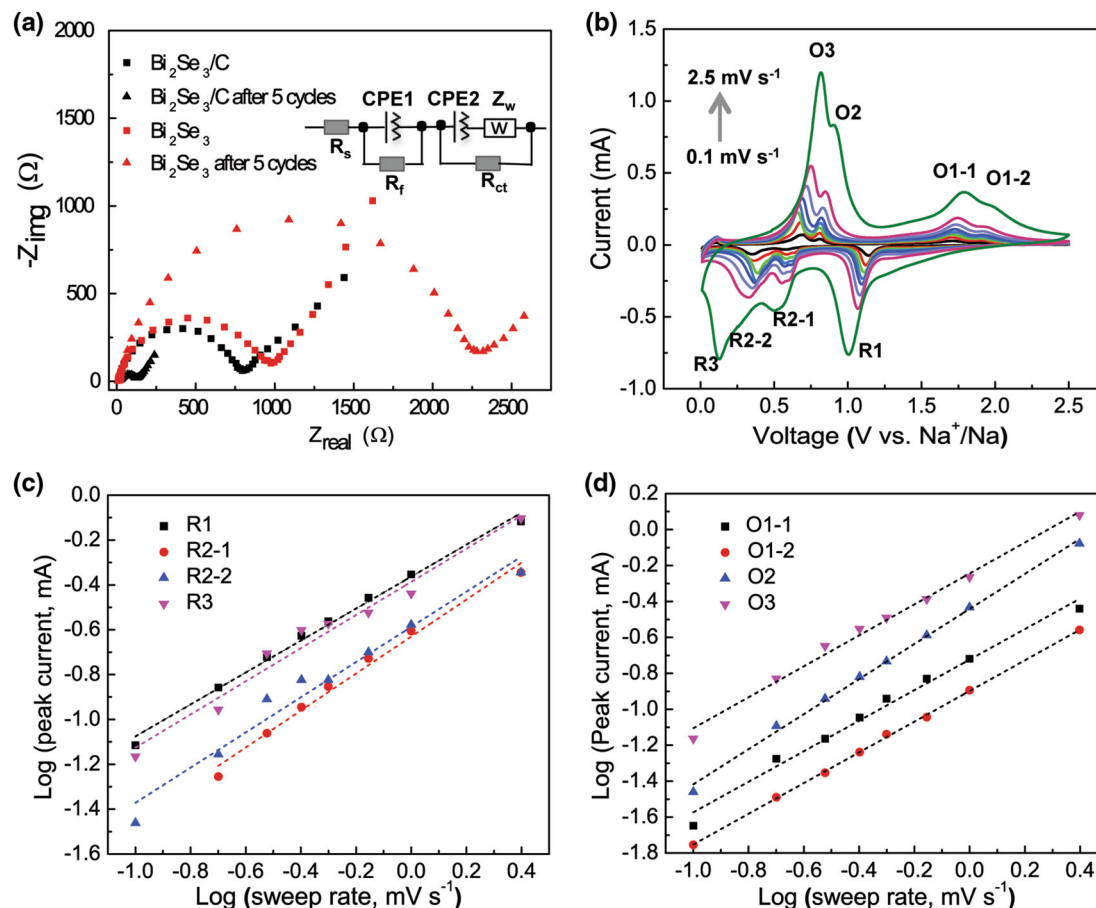**Fig. 5** **a** EIS spectra for Bi_2Se_3 and Bi_2Se_3/C anodes before and after five cycles. **b** CV curves of the Bi_2Se_3/C anode at different scan rates. **c, d** *b*-value fitted by the relationship of the logarithm peak currents and logarithm scan rates

$log(v)$ at the corresponding peaks derived from the *I–V* curves are shown in Fig. 5c, d. The fitted *b* values are 0.71, 0.82, 0.78, and 0.74 for the R_1, R_{2-1}, R_{2-2}, R_3 peaks and 0.85, 0.85, 0.98, and 0.86 for O_{1-1}, O_{1-2}, O_2, and O_3 peaks. These values are much higher than 0.5, which indicates that fast capacitive process occurs during Na storage, contributing to the high rate capacity for the Bi_2Se_3/C electrode. The current and scan rate relations are not shown for Bi_2Se_3 electrode because of the significant changes of the CV curves over cycling.

4 Conclusions

The application of Bi_2Se_3 was explored as an anode material for SIBs. Benefiting from the high theoretical capacity and high intrinsic conductivity of Bi_2Se_3, the positive effects of carbon, and the effective HEBM method, a high-performance anode material was achieved. The Bi_2Se_3/C electrode showed a high reversible capacity of 527 mAh g^{-1} and retains 89% of this capacity over 100 cycles at 0.1 A g^{-1}. To obtain insights regarding the electrochemical process of Na storage, the phase changes were revealed by ex situ XRD.

References

1. V. Palomares, P. Serras, I. Villaluenga, K.B. Hueso, J. Carretero-González, T. Rojo, Na-ion batteries, recent advances and present challenges to become low cost energy storage systems. Energy

Environ. Sci. **5**(3), 5884–5901 (2012). https://doi.org/10.1039/c2ee02781j

2. H. Kim, H. Kim, Z. Ding, M.H. Lee, K. Lim, G. Yoon, K. Kang, Recent progress in electrode materials for sodium-ion batteries. Adv. Energy Mater. **6**(19), 1600943 (2016). https://doi.org/10.1002/aenm.201600943

3. S. Chu, Y. Cui, N. Liu, The path towards sustainable energy. Nat. Mater. **16**(1), 16–22 (2016). https://doi.org/10.1038/nmat4834

4. Z. Yang, Y. Jiang, L. Deng, T. Wang, S. Chen, Y. Huang, A high-voltage honeycomb-layered Na_4NiTeO_6 as cathode material for Na-ion batteries. J. Power Sources **360**, 319–323 (2017). https://doi.org/10.1016/j.jpowsour.2017.06.014

5. C.P. Grey, J.M. Tarascon, Sustainability and in situ monitoring in battery development. Nat. Mater. **16**(1), 45–56 (2016). https://doi.org/10.1038/nmat4777

6. N. Yabuuchi, K. Kubota, M. Dahbi, S. Komaba, Research development on sodium-ion batteries. Chem. Rev. **114**(23), 11636–11682 (2014). https://doi.org/10.1021/cr500192f

7. M. Lao, Y. Zhang, W. Luo, Q. Yan, W. Sun, S.X. Dou, Alloy-based anode materials toward advanced sodium-ion batteries. Adv. Mater. **29**(48), 1700622 (2017). https://doi.org/10.1002/adma.201700622

8. L.D. Ellis, B.N. Wilkes, T.D. Hatchard, M.N. Obrovac, In situ XRD study of silicon, lead and bismuth negative electrodes in nonaqueous sodium cells. J. Electrochem. Soc. **161**(3), A416–A421 (2014). https://doi.org/10.1149/2.080403jes

9. C. Wang, L. Wang, F. Li, F. Cheng, J. Chen, Bulk bismuth as a high-capacity and ultralong cycle-life anode for sodium-ion batteries by coupling with glyme-based electrolytes. Adv. Mater. **29**(35), 1702212 (2017). https://doi.org/10.1002/adma.201702212

10. M.M. Doeff, Y. Ma, S.J. Visco, L.C.D. Jonghe, Electrochemical insertion of sodium into carbon. J. Electrochem. Soc. **140**(12), 169–170 (1993). https://doi.org/10.1149/1.2221153

11. S. Komaba, W. Murata, T. Ishikawa, N. Yabuuchi, T. Ozeki, T. Nakayama, A. Ogata, K. Gotoh, K. Fujiwara, Electrochemical Na insertion and solid electrolyte interphase for hard-carbon electrodes and application to Na-ion batteries. Adv. Funct. Mater. **21**(20), 3859–3867 (2011). https://doi.org/10.1002/adfm.201100854

12. Y. Li, Y.-S. Hu, M.-M. Titirici, L. Chen, X. Huang, Hard carbon microtubes made from renewable cotton as high-performance anode material for sodium-ion batteries. Adv. Energy Mater. **6**(18), 1600659 (2016). https://doi.org/10.1002/aenm.201600659

13. M. Dahbi, N. Yabuuchi, K. Kubota, K. Tokiwa, S. Komaba, Negative electrodes for Na-ion batteries. Phys. Chem. Chem. Phys. **16**(29), 15007–15028 (2014). https://doi.org/10.1039/c4cp00826j

14. D. Su, S. Dou, G. Wang, Bismuth: a new anode for the Na-ion battery. Nano Energy **12**, 88–95 (2015). https://doi.org/10.1016/j.nanoen.2014.12.012

15. Z. Hu, Q. Liu, S.-L. Chou, S.-X. Dou, Advances and challenges in metal sulfides/selenides for next-generation rechargeable sodium-ion batteries. Adv. Mater. **29**(48), 1700606 (2017). https://doi.org/10.1002/adma.201700606

16. Z. Liu, T. Lu, T. Song, X.-Y. Yu, X.W. Lou, U. Paik, Structure-designed synthesis of FeS_2@C yolk–shell nanoboxes as a high-performance anode for sodium-ion batteries. Energy Environ. Sci. **10**(7), 1576–1580 (2017). https://doi.org/10.1039/c7ee01100h

17. Y. Kim, Y. Kim, Y. Park, Y.N. Jo, Y.J. Kim, N.S. Choi, K.T. Lee, SnSe alloy as a promising anode material for Na-ion batteries. Chem. Commun. **51**(1), 50–53 (2015). https://doi.org/10.1039/c4cc06106c

18. X. Duan, J. Xu, Z. Wei, J. Ma, S. Guo, H. Liu, S. Dou, Atomically thin transition-metal dichalcogenides for electrocatalysis

and energy storage. Small Methods **1**(11), 1700156 (2017). https://doi.org/10.1002/smtd.201700156

19. W. Sun, X. Rui, D. Zhang, Y. Jiang, Z. Sun, H. Liu, S. Dou, Bismuth sulfide: a high-capacity anode for sodium-ion batteries. J. Power Sources **309**, 135–140 (2016). https://doi.org/10.1016/j.jpowsour.2016.01.092

20. W. Yang, H. Wang, T. Liu, L. Gao, A Bi_2S_3@CNT nanocomposite as anode material for sodium ion batteries. Mater. Lett. **167**, 102–105 (2016). https://doi.org/10.1016/j.matlet.2015.12.108

21. W. Liu, K.C. Lukas, K. McEnaney, S. Lee, Q. Zhang, C.P. Opeil, G. Chen, Z. Ren, Studies on the Bi_2Te_3–Bi_2Se_3–Bi_2S_3 system for mid-temperature thermoelectric energy conversion. Energy Environ. Sci. **6**(2), 552–560 (2013). https://doi.org/10.1039/c2ee23549h

22. Y. Lu, P. Zhou, K. Lei, Q. Zhao, Z. Tao, J. Chen, Selenium phosphide (Se_4P_4) as a new and promising anode material for sodium-ion batteries. Adv. Energy Mater. **7**(7), 1601973 (2017). https://doi.org/10.1002/aenm.201601973

23. H. Xu, G. Chen, R. Jin, J. Pei, Y. Wang, D. Chen, Hierarchical Bi_2Se_3 microrods: microwave-assisted synthesis, growth mechanism and their related properties. CrystEngComm **15**(8), 1618–1625 (2013). https://doi.org/10.1039/c2ce26678d

24. Z. Ali, C. Cao, J. Li, Y. Wang, T. Cao, M. Tanveer, M. Tahir, F. Idrees, F.K. Butt, Effect of synthesis technique on electrochemical performance of bismuth selenide. J. Power Sources **229**, 216–222 (2013). https://doi.org/10.1016/j.jpowsour.2012.11.120

25. F. Mao, J. Guo, S. Zhang, F. Yang, Q. Sun, J. Ma, Z. Li, Solvothermal synthesis and electrochemical properties of S-doped Bi_2Se_3 hierarchical microstructure assembled by stacked nanosheets. RSC Adv. **6**(44), 38228–38232 (2016). https://doi.org/10.1039/c6ra01301e

26. R. Jin, J. Liu, Y. Xu, G. Li, G. Chen, L. Yang, Hierarchical Bi_2Se_3–xS_x microarchitectures assembled from ultrathin polycrystalline nanosheets: solvothermal synthesis and good electrochemical performance. J. Mater. Chem. A **1**(36), 10942 (2013). https://doi.org/10.1039/c3ta12030a

27. G. Han, Z.-G. Chen, D. Ye, L. Yang, L. Wang, J. Drennan, J. Zou, In-doped Bi_2Se_3 hierarchical nanostructures as anode materials for Li-ion batteries. J. Mater. Chem. A **2**(19), 7109–7116 (2014). https://doi.org/10.1039/c4ta00045e

28. Y. Liu, N. Zhang, L. Jiao, Z. Tao, J. Chen, Ultrasmall Sn nanoparticles embedded in carbon as high-performance anode for sodium-ion batteries. Adv. Funct. Mater. **25**(2), 214–220 (2015). https://doi.org/10.1002/adfm.201402943

29. Y. Kim, Y. Kim, A. Choi, S. Woo, D. Mok et al., Tin phosphide as a promising anode material for Na-ion batteries. Adv. Mater. **26**(24), 4139–4144 (2014). https://doi.org/10.1002/adma.201305638

30. J. Duan, W. Zhang, C. Wu, Q. Fan, W. Zhang, X. Hu, Y. Huang, Self-wrapped Sb/C nanocomposite as anode material for high-performance sodium-ion batteries. Nano Energy **16**, 479–487 (2015). https://doi.org/10.1016/j.nanoen.2015.07.021

31. Y.N. Ko, Y.C. Kang, Electrochemical properties of ultrafine Sb nanocrystals embedded in carbon microspheres for use as Na-ion battery anode materials. Chem. Commun. **50**(82), 12322–12324 (2014). https://doi.org/10.1039/c4cc05275g

32. Z. Yang, J. Sun, Y. Ni, Z. Zhao, J. Bao, S. Chen, Facile synthesis and in situ transmission electron microscopy investigation of a highly stable Sb_2Te_3/C nanocomposite for sodium-ion batteries. Energy Storage Mater. **9**, 214–220 (2017). https://doi.org/10.1016/j.ensm.2017.07.010

33. S. Ni, J. Ma, J. Zhang, X. Yang, L. Zhang, Electrochemical performance of cobalt vanadium oxide/natural graphite as anode for lithium ion batteries. J. Power Sources **282**, 65–69 (2015). https://doi.org/10.1016/j.jpowsour.2015.01.187

34. J. Ma, S. Ni, J. Zhang, X. Yang, L. Zhang, The charge/discharge mechanism and electrochemical performance of CuV_2O_6 as a new anode material for Li-ion batteries. Phys. Chem. Chem. Phys. **17**(33), 21442–21447 (2015). https://doi.org/10.1039/c5cp03435c

35. Q. Wang, W. Zhang, C. Guo, Y. Liu, C. Wang, Z. Guo, In situ construction of 3D interconnected $FeS@Fe_3C@$graphitic carbon networks for high-performance sodium-ion batteries. Adv. Funct. Mater. **27**(41), 1703390 (2017). https://doi.org/10.1002/adfm.201703390

36. Q. Wang, C. Guo, Y. Zhu, J. He, H. Wang, Reduced graphene oxide-wrapped FeS_2 composite as anode for high-performance sodium-ion batteries. Nano-Micro Lett. **10**, 30 (2018). https://doi.org/10.1007/s40820-017-0183-z

37. J. Liang, X. Gao, J. Guo, C. Chen, K. Fan, J. Ma, Electrospun $MoO_2@NC$ nanofibers with excellent Li^+/Na^+ storage for dual applications. Sci. China Mater. **61**(1), 30–38 (2017). https://doi.org/10.1007/s40843-017-9119-2

38. J. Liang, C. Yuan, H. Li, K. Fan, Z. Wei, H. Sun, J. Ma, Growth of SnO_2 nanoflowers on N-doped carbon nanofibers as anode for Li- and Na-ion batteries. Nano-Micro Lett. **10**(2), 21 (2018). https://doi.org/10.1007/s40820-017-0172-2

39. Y. Zhou, W. Sun, X. Rui, Y. Zhou, W.J. Ng, Q. Yan, E. Fong, Biochemistry-derived porous carbon-encapsulated metal oxide nanocrystals for enhanced sodium storage. Nano Energy **21**, 71–79 (2016). https://doi.org/10.1016/j.nanoen.2015.12.003

40. X. Zhang, Y. Zhou, B. Luo, H. Zhu, W. Chu, K. Huang, Microwave-assisted synthesis of $NiCo_2O_4$ double-shelled hollow spheres for high-performance sodium Ion batteries. Nano-Micro Lett. **10**(1), 13 (2017). https://doi.org/10.1007/s40820-017-0164-2

41. M. Mao, C. Cui, M. Wu, M. Zhang, T. Gao et al., Flexible ReS_2 nanosheets/N-doped carbon nanofibers-based paper as a universal anode for alkali (Li, Na, K) ion battery. Nano Energy **45**, 346–352 (2018). https://doi.org/10.1016/j.nanoen.2018.01.001

42. F. Yang, F. Yu, Z. Zhang, K. Zhang, Y. Lai, J. Li, Bismuth nanoparticles embedded in carbon spheres as anode materials for sodium/lithium-ion batteries. Chem.-Eur. J. **22**(7), 2333–2338 (2016). https://doi.org/10.1002/chem.201503272

43. J. Sottmann, M. Herrmann, P. Vajeeston, Y. Hu, A. Ruud, C. Drathen, H. Emerich, H. Fjellvåg, D.S. Wragg, How crystallite size controls the reaction path in nonaqueous metal ion batteries: the example of sodium bismuth alloying. Chem. Mater. **28**(8), 2750–2756 (2016). https://doi.org/10.1021/acs.chemmater.6b00491

44. D. Kong, J.J. Cha, K. Lai, H. Peng, J.G.A.S. Meister et al., Rapid surface oxidation as a source of surface degradation factor for Bi_2Se_3. ACS Nano **5**(6), 4698–4703 (2011). https://doi.org/10.1021/nn200556h

45. S.R. Leadley, J.F. Watts, The use of XPS to examine the interaction of poly(acrylic acid) with oxidised metal substrates. J. Electron Spectrosc. **85**(1–2), 107–121 (1997). https://doi.org/10.1016/S0368-2048(97)00028-5

46. F.A. Soto, P. Yan, M.H. Engelhard, A. Marzouk, C. Wang et al., Tuning the solid electrolyte interphase for selective Li- and Na-ion storage in hard carbon. Adv. Mater. **29**(18), 1606860 (2017). https://doi.org/10.1002/adma.201606860

47. S. Ni, J. Zhang, J. Ma, X. Yang, L. Zhang, X. Li, H. Zeng, Approaching the theoretical capacity of Li_3VO_4 via electrochemical reconstruction. Adv. Mater. Interfaces **3**(1), 1500340 (2016). https://doi.org/10.1002/admi.201500340

48. S. Ni, J. Ma, J. Zhang, X. Yang, L. Zhang, Excellent electrochemical performance of $NiV_3O_8/$natural graphite anodes via novel in situ electrochemical reconstruction. Chem. Commun. **51**(27), 5880–5882 (2015). https://doi.org/10.1039/c5cc00486a

49. J. Wang, J. Polleux, J. Lim, B. Dunn, Pseudocapacitive contributions to electrochemical energy storage in TiO_2 (anatase) nanoparticles. J. Phys. Chem. C **111**(40), 14925–14931 (2007). https://doi.org/10.1021/jp074464w

50. C. Chen, Y. Wen, X. Hu, X. Ji, M. Yan, L. Mai, P. Hu, B. Shan, Y. Huang, Na^+ intercalation pseudocapacitance in graphene-coupled titanium oxide enabling ultra-fast sodium storage and long-term cycling. Nat. Commun. **6**, 6929 (2015). https://doi.org/10.1038/ncomms7929

51. X. Deng, Z. Wei, C. Cui, Q. Liu, C. Wang, J. Ma, Oxygen-deficient anatase $TiO_2@C$ nanospindles with pseudocapacitive contribution for enhancing lithium storage. J. Mater. Chem. A **6**(9), 4013–4022 (2018). https://doi.org/10.1039/c7ta11301c